Check for updates

View Article Online
View Journal

Journal of
Materials Chemistry A

Materials for energy and sustainability

Accepted Manuscript

This article can be cited before page numbers have been issued, to do this please use: Y. Shuang, Y. Saito, S. Hatayama, M. Kim, P. Fons and Y. Sutou, *J. Mater. Chem. A*, 2026, DOI: 10.1039/D5TA10269C.

This is an Accepted Manuscript, which has been through the Royal Society of Chemistry peer review process and has been accepted for publication.

Accepted Manuscripts are published online shortly after acceptance, before technical editing, formatting and proof reading. Using this free service, authors can make their results available to the community, in citable form, before we publish the edited article. We will replace this Accepted Manuscript with the edited and formatted Advance Article as soon as it is available.

You can find more information about Accepted Manuscripts in the Information for Authors.

Please note that technical editing may introduce minor changes to the text and/or graphics, which may alter content. The journal's standard Terms & Conditions and the Ethical guidelines still apply. In no event shall the Royal Society of Chemistry be held responsible for any errors or omissions in this Accepted Manuscript or any consequences arising from the use of any information it contains.

ROYAL SOCIETY OF CHEMISTRY

rsc.li/materials-a

View Article Online
DOI: 10.1039/D5TA10269C

ARTICLE

Residual Oxygen–Driven P–N Conversion and Thermoelectric Properties in CrN Films

Received 00th January 20xx,
Accepted 00th January 20xx

DOI: 10.1039/x0xx00000x

Yi Shuang*[a,b], Yuta Saito[a,c], Shogo Hatayama[d], Mihyeon Kim[a], Fons Paul[e] and Yuji Sutou*[a,b]

Transition metal nitrides such as CrN are promising for thermoelectric applications due to their high stability and tunable electronic properties, yet they have been largely limited to *n*-type conduction, restricting device design. Here, we report the successful synthesis of *p*-type CrN films via controlled residual oxygen incorporation during RF magnetron sputtering regulated through N_2 gas flow adjustment, without introducing any additional oxygen source. Low N_2 gas flow rate (f_{N2}) produces N-deficient $CrN_{1-\delta}$(O) films with *n*-type conduction dominated by nitrogen vacancies, while higher f_{N2} (≥4 sccm) stabilizes Cr vacancies in over-stoichiometric $Cr_{1-\delta}$N(O) films, resulting in *p*-type hole conduction. Cr K-edge X-ray absorption fine structure (XAFS) reveals Cr–Cr bond elongation, reduced coordination, and enhanced Cr3*d*-O/N2*p* hybridization, indicative of localized hole states. Temperature-dependent transport measurements confirm the mechanisms, leading to a room-temperature power factor (PF) of up to 0.105 $mW\cdot m^{-1}\cdot K^{-2}$ (*n*-type) and 0.053 $mW\cdot m^{-1}\cdot K^{-2}$ (*p*-type). The structural similarity between the *n*- and *p*-type films enables the creation of p–n homojunctions, highlighting a straightforward route for CrN-based thermoelectric devices.

Introduction

Thermoelectric (TE) materials have emerged as key enablers for sustainable energy technologies, as they can directly convert waste heat into electrical energy without any moving parts or greenhouse emissions.[1] The energy conversion efficiency of a thermoelectric material is characterized by the dimensionless figure of merit, $ZT = S^2\sigma T/\kappa$, where S denotes the Seebeck coefficient, σ the electrical conductivity, and κ the thermal conductivity.[2,3] A high ZT thus requires the simultaneous enhancement of the power factor PF ($S^2\sigma$) and the suppression of heat transport. In the past decades, extensive efforts have been devoted to improving bulk TE materials such as Bi_2Te_3, PbTe, and SnSe.[4] While these compounds have demonstrated outstanding ZT values near or above unity, their practical applications are constrained by scarcity, toxicity, or poor thermal and chemical stability, particularly at elevated temperatures. Recently, thin film thermoelectric devices have drawn growing interest due to their versatility in microelectronic integration and localized energy harvesting. Film configurations offer additional advantages such as microstructural engineering, strain modulation, and controlled carrier transport across nanoscale interfaces.[5] These properties make TE films attractive for emerging applications, including flexible temperature sensors[6], microscale power generation applications[7] and on-chip energy harvesting devices[8]. Nevertheless, most conventional telluride-based TE films are chemically unstable, corrode easily, and degrade under thermal cycling, severely limiting their operational reliability at high temperatures.[9,10]

In this context, transition-metal nitrides (TMNs) and rare-earth nitrides (RENs) have been identified as promising candidates for robust thermoelectric films.[11–14] They possess high mechanical strength, excellent oxidation and corrosion resistance, moderate thermal conductivity, and a broad tunability in electrical transport properties. Among TMNs, chromium nitride (CrN) stands out as an *n*-type semiconductor with intriguing electronic and thermal characteristics. CrN exhibits relatively low resistivity together with the large Seebeck coefficient around 120 μV/K, resulting in a competitive power factor.[15,16] Furthermore, the high melting point and chemical inertness of CrN enable stable operation under harsh thermal environments, making it suitable for high-temperature TE applications.[17] The *n*-type conduction in CrN mainly originates from nitrogen vacancies within its rocksalt structure, which provide donor-like states near the conduction band. [18] In addition, the intrinsic lattice instabilities of the rocksalt CrN phase contribute to a suppressed lattice thermal conductivity, a beneficial feature for thermoelectric performance. [15,19] Given the intrinsic low thermal conductivity of CrN, enhancing its ZT primarily relies on increasing the power factor through modulation of carrier concentration and carrier scattering mechanisms. The narrow bandgap with the range of 0~0.7 eV and high defect tolerance of CrN allow its electrical properties to be tuned from metallic to semiconducting regimes through compositional control and defect engineering.16,20–23 However, for practical TE module design, both *n*- and *p*-type materials are essential. Ideally, these two components should

[a.] Department of Material Science, Graduate School of Engineering, Tohoku University, 6-6-11, Aoba-yama, Aoba-ku, Sendai 980-8579, Japan.
[b.] WPI Advanced Institute for Materials Research, Tohoku University, 2-1-1 Katahira, Aoba-ku, Sendai 980-8577, Japan.
[c.] Research Center for Green X-Tech, Tohoku University, 6-6-11, Aoba-yama, Aoba-ku, Sendai 980-8579, Japan
[d.] Semiconductor Frontier Research Center, National Institute of Advanced Industrial Science and Technology (AIST), Tsukuba, 305- 8568, Japan.
[e.] Department of Electronics and Electrical Engineering, Faculty of Science and Technology, Keio University, 3-14-1 Hiyoshi, Kohoku-ku, Yokohama, Kanagawa 223-8522, Japan

Open Access Article. Published on 06 March 2026. Downloaded on 3/7/2026 11:28:15 PM.
This article is licensed under a Creative Commons Attribution 3.0 Unported Licence.

Journal of Materials Chemistry A Accepted Manuscript

View Article Online
DOI: 10.1039/D5TA10360C

possess similar crystal structures, thermal expansion coefficients, and mechanical properties to minimize interfacial strain and chemical interdiffusion.[24,25] One straightforward strategy is to achieve both *n*- and *p*-type conduction in a single material system. In this regard, *p*-type conduction in CrN has been reported to occur through metal-site substitutional doping. For example, alloying CrN with aluminium has been shown to induce a transition from *n*-type to *p*-type conduction, which was initially attributed to the substitution of Al for Cr and the associated modification of the electronic structure.[26] More recently, Mg-doped CrN has also been demonstrated to exhibit *p*-type behaviour. Density functional theory (DFT) calculations revealed that Mg substitution on the Cr site shifts the electronic bands upward such that the Fermi level enters the valence band, thereby inducing hole carriers.[27] These studies indicate that *p*-type transport in CrN can be achieved through appropriate substitutional metal doping via intrinsic band-structure modification.

Beyond intentional substitutional doping, subsequent studies have revealed that carrier polarity in CrN is highly sensitive to deviations from stoichiometry and native defect chemistry. In particular, Le Febvrier et al. demonstrated that the *n*–*p* type transition in CrN is primarily governed by the overall anion/cation ratio and the formation of Cr vacancies under nitrogen-rich conditions.[28] Their combined experimental and theoretical analysis showed that *p*-type conduction emerges when metal-site vacancies become dominant, while oxygen contamination at the 1–2% level mainly shifts the apparent transition point away from the ideal stoichiometric limit. Although theory predicts the transition to occur at zero deviation from stoichiometry, experimentally observed switching at $CrN_{1+\delta}$ with $\delta \approx -0.03$ highlights the strong sensitivity of carrier polarity to subtle changes in defect chemistry. Within this framework, oxygen incorporation should be considered as an important compositional factor that influences defect equilibria in TMN thin films, rather than as a direct acceptor itself. In reactive sputtering processes, oxygen contamination is difficult to control: even a slight partial pressure of oxygen, such as 3.0×10^{-3} Pa relative to a working pressure of 1.0 Pa , almost 40 at.% oxygen can be incorporated into the growing TiN film.[29] Depending on the concentration, oxygen atoms will substitute for nitrogen sites or occupy interstitial positions, thereby acting as donors or acceptors and strongly affecting carrier polarity and mobility. Exploiting this unavoidable oxygen incorporation, rather than eliminating it, should provide a new approach for tuning the transport properties in, especially, semiconducting nitride films.

In this study, we demonstrate an oxygen-driven *n*–*p* conversion in CrN films achieved without any external oxygen source. Instead, we utilize the residual oxygen naturally present in the sputtering chamber and reproducible control its incorporation by fixing the chamber base pressure at 10^{-5} Pa and simply adjusting the nitrogen gas flow rate (f_{N2}) and the working pressure during radio-frequency (RF) magnetron sputtering. This straightforward yet highly effective approach enables accurate control of oxygen content, from 6.8 to 12.4 at.% by just varying f_{N2} from 2 to 8 sccm, and consequently, leading to a transition of CrN from *n*- to *p*-type conduction. The structural, electrical, and thermoelectric characteristics of the resulting CrN(O) (Hereafter, the oxygen-incorporated CrN films are referred to as CrN(O) for simplicity) films were comprehensively investigated, revealing a strong correlation between oxygen incorporation and charge transport. This work provides a simple, cost-effective, and large-area-compatible strategy to tune carrier polarity in transition-metal nitrides, offering new insights into defect-mediated thermoelectric design.

Experimental

Preparation of CrN(O) films

CrN(O) films were deposited on Si/SiO_2 (100 nm) or quartz substrates by RF magnetron reactive sputtering of Cr (99.99%) pure targets at room temperature (R.T.) in an Ar (99.999 vol.%)/ N_2 (99.999 vol.%) atmosphere. The RF power of Cr was fixed at 50 W. The Ar gas flow rate was fixed at 15 sccm and the N_2 gas flow rate (f_{N2}) varied from 0 to 10 sccm. The base pressure of the sputtering chamber was fixed at approximately 10^{-5} Pa. The working pressure during sputtering was around 0.34 Pa without flowing N_2 gas, and increased up to 0.54 Pa when the f_{N2} flow was set to 10 sccm. The film thickness was measured by Atomic Force Microscopy (AFM).

Characterization of CrN(O) films

The stoichiometry of the films deposited at f_{N2} values of 2, 6, 8 sccm were determined by Rutherford backscattering (RBS, Pelletron 3SDH, National Electrostatics Corporation) using 2300 keV He ions at a scattering angle of 160 and 104°, respectively. The films for RBS measurements were deposited on Si/SiO_2 (100 nm) substrates with a thickness of 30 nm. To prevent surface oxidation, a 5 nm Cr cap layer was *in-situ* deposited in the same sputtering chamber. The resulting compositional depth profiles from surface to substrate are shown in **Figure 1(a)**. It can be observed that, even with the 5 nm Cr cap, slight oxidation occurs near the interface between the CrN(O) film and the cap; however, the composition becomes uniform at greater depths, indicating the intrinsic presence of a small amount of oxygen in the CrN(O) films during sputtering. The elemental compositions were taken from the flat region of the depth profiles and are summarized in **Table 1**. A small amount of oxygen was confirmed in all films, and the oxygen content increased with increasing f_{N2} and the associated working pressure. Since ultra-high purity argon (G1, O_2 < 0.1 vol.ppm) or nitrogen (G1, O_2 < 0.1 vol.ppm) gas was used, the oxygen incorporation discussed in this work arises from unavoidable residual oxygen in the sputtering system and is controlled indirectly through process parameters rather than by intentional oxygen dosing.

Table 1. Composition of the CrN(O) films determined by RBS.

f_{N2} (sccm)	Cr (at. %)	N (at. %)	O (at. %)	Working pressure (Pa)
2	54.7	39.3	6.0	0.38
6	47.5	43.9	8.6	0.46
8	45.3	42.3	12.4	0.50

The crystal structures of the as-deposited CrN(O) films were investigated by X-ray diffraction (XRD, Rigaku; Ultima IV). The diffraction patterns were taken in the 2θ range from 35° to 50° with Cu Kα radiation. Quartz substrates were used for XRD measurements. The cross-sectional microstructure of CrN(O) films were observed using field emission transmission electron microscope (FE-TEM, HF-

Open Access Article. Published on 06 March 2026. Downloaded on 3/7/2026 11:28:15 PM.
This article is licensed under a Creative Commons Attribution 3.0 Unported Licence.

Journal of Materials Chemistry A Accepted Manuscript

This journal is © The Royal Society of Chemistry 20xx

Please do not adjust margins

View Article Online
DOI: 10.1039/D5TA10260C

2000EDX; Hitachi) at an accelerating voltage of 200 kV. TEM samples of the CrN(O) films were thinned using ion milling (PIPS; Gatan). X-ray photoelectron spectroscopy (XPS, Thermo VG; Theta Probe) was performed to analyze the chemical bonding state of elements in the CrN(O) films. Ar ion etching for 60 min with a 1 kV ion gun was carried out to remove the surface oxidation layer before the XPS measurements. All energies were calibrated using the C 1*s* peak at 285.0 eV. The films for TEM and XPS measurement were deposited on Si/SiO_2 (100 nm) substrates. X-ray absorption fine structure (XAFS) measurements were carried out at beamline BL01B1 at SPring-8 of the Japan Synchrotron Radiation Research Institute (JASRI). Cr K-edge spectra were recorded in fluorescence mode.100-nm-thick CrN(O) films at f_{N2} of 2, 4 and 6 sccm were deposited onto quartz substrates for the measurements. A 5-nm-thick SiO_2 layer was deposited on the surface of the CrN(O) films to prevent surface oxidation. The XAFS data obtained were analyzed using Athena and Artemis software.[30] The electrical properties of the film were evaluated by Hall-effect measurements (Toyo Corp.; ResiTest 8400). The temperature dependence of the resistivity for the CrN(O) films was investigated under He ambient by the van der Pauw method. The temperature range was set to be 250-400 K with a step of 10 K. AC Hall measurements (Toyo Corp.; ResiTest 8400) were carried out to measure the Hall properties at RT in the same chamber as used for the resistivity measurements. The Seebeck coefficient *S* was measured (Toyo Corp.; ResiTest 8300) over the temperature range of 260-400 K. The above electrical characterizations were carried out on uncapped CrN films immediately after film growth. Insulating quartz substrates were selected to avoid any unwanted parallel conduction paths during the electrical measurements. The thermal conductivity of selected CrN(O) thin films was measured using time-domain thermoreflectance (TDTR) technique (PicoTR system; NETZSCH).

First-Principles Calculations

The first-principles calculations of CrN films with oxygen incorporated were carried out using Density Functional Theory (DFT) calculations. These calculations were conducted using the Vienna Ab-initio Simulation Package (VASP) and projector augmented plane wave (PAW) pseudopotentials, with the Perdew-Burke-Ernzerhof (PBE) generalized gradient approximation (GGA) for handling exchange and correlation effects. Several possible crystal model candidates with different defect states were considered using 3 × 3 × 3 supercells of cubic CrN (Fm-3m). Each system was fully relaxed. The plane-wave cut-off energy was set at 400 eV.

Results and discussion

Structural analysis

Figure 1(b) shows the atomic ratio of O/Cr, N/Cr and (O+N)/Cr calculated from the RBS results for the CrN(O) films. The CrN(O) film deposited at f_{N2} = 2 sccm was off-stoichiometric with a N/Cr ratio less than 1 and an oxygen content of around 6.0 at. % ($CrN_{0.72}O_{0.11}$). Since

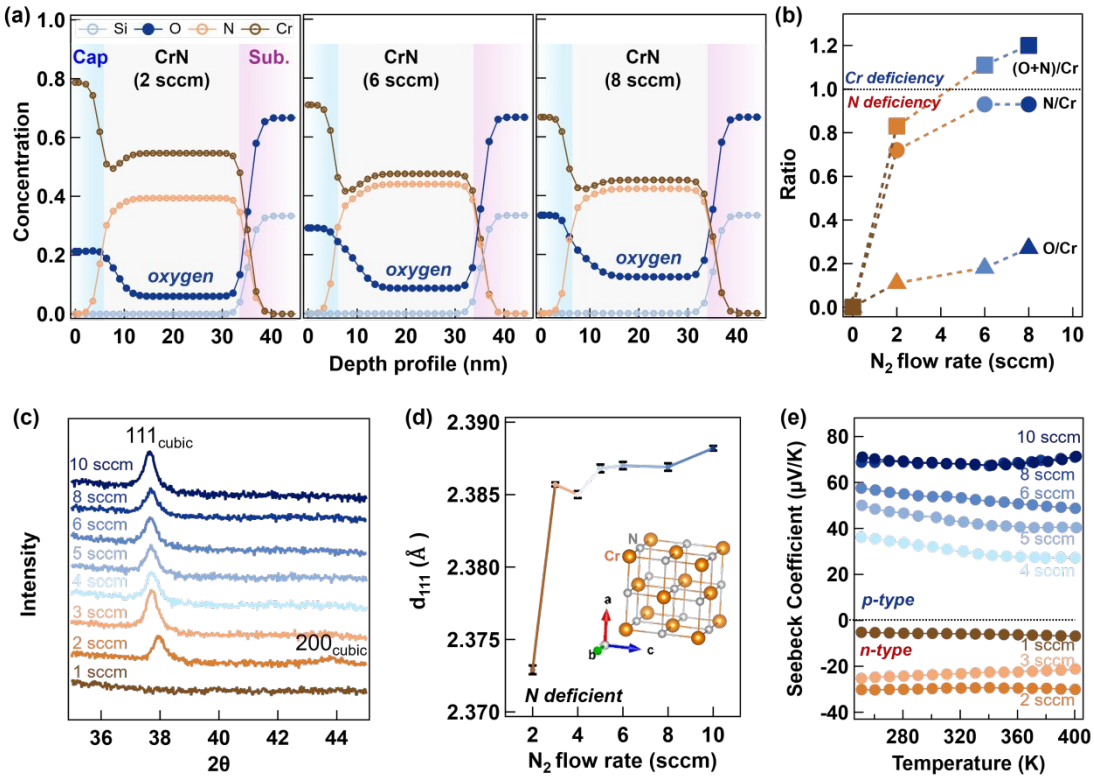

Figure 1. (a) Concentration depth profile of Si, O, Cr, N in CrN(O) films deposited at f_{N2} of 2, 6, 8 sccm measured from RBS. **(b)** The atomic ratio of O/Cr, N/Cr and (O+N)/Cr calculated from RBS results taken from the uniform part of the depth profile. **(c)** XRD patterns, **(d)** $d_{(111)}$ and **(e)** Temperature dependent of Seebeck coefficient of the CrN(O) films at various f_{N2}.

Open Access Article. Published on 06 March 2026. Downloaded on 3/7/2026 11:28:15 PM.
This article is licensed under a Creative Commons Attribution 3.0 Unported Licence.

Journal of Materials Chemistry A Accepted Manuscript

Please do not adjust margins

View Article Online
DOI: 10.1039/D5TA10269C

Open Access Article. Published on 06 March 2026. Downloaded on 3/7/2026 11:28:15 PM.
This article is licensed under a Creative Commons Attribution 3.0 Unported Licence.

Journal of Materials Chemistry A Accepted Manuscript

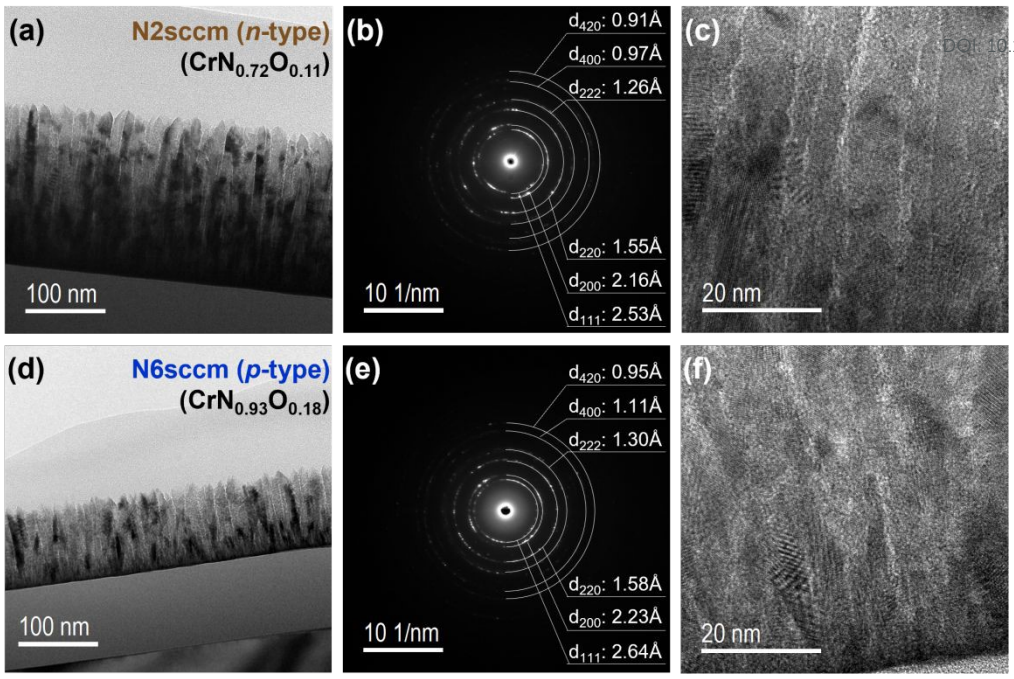

Figure 2. Cross-sectional TEM image of a CrN(O) film deposited at a f_{N2} of **(a)** 2 sccm ($CrN_{0.72}O_{0.11}$) and **(d)** 6 sccm ($CrN_{0.93}O_{0.18}$). Diffraction patterns and indexing of **(b)** $CrN_{0.72}O_{0.11}$ and **(e)** $CrN_{0.93}O_{0.18}$ film. STEM images of **(c)** $CrN_{0.72}O_{0.11}$ and **(f)** $CrN_{0.93}O_{0.18}$ film.

the Ar flow rate was fixed at 15 sccm, the increase in f_{N2} raised the working pressure, leading to a higher oxygen partial pressure and consequently leading to increased oxygen content in the films. Similar behavior was observed in zinc oxy-nitride films, where the oxygen concentration was found to increase with working pressure.[31] For f_{N2} values above 6 sccm, the N/Cr ratio approached 1, but the total N+O concentration exceeded the Cr concentration, indicating Cr-deficiency. Specifically, the CrN(O) films deposited for f_{N2} = 6 and 8 sccm contained ~8.6 at. % O ($CrN_{0.93}O_{0.18}$), and ~12.4 at. % O ($CrN_{0.93}O_{0.27}$), respectively. **Figure 1(c)** shows XRD patterns of the as-grown films at R.T., illustrating the phase evolution as a function of f_{N2}. At f_{N2} = 1 sccm, the reflection peaks are very weak, suggesting a very fine microstructure and the coexistence of multiple minor phases such as Cr or Cr_2N in addition to CrN. When f_{N2} exceeds 2 sccm, the NaCl-type cubic CrN phase begins to form. At this stage, 111_{cubic} and 200_{cubic} reflections appear at relatively higher angles, indicating a reduced lattice constant due to insufficient nitrogen content and the presence of numerous nitrogen vacancies. For $f_{N2} \geqq$ 3 sccm, the NaCl-type cubic phase exhibits a pronounced (111) preferred orientation parallel to the substrate, with the 111_{cubic} peak gradually shifting to lower angles with increasing f_{N2}, reflecting lattice expansion as nitrogen atoms occupy previously vacant sites. The peak positions and intensities remain essentially unchanged for $f_{N2} \geqq$ 3 sccm, suggesting the nitrogen content approaches saturation and stoichiometric CrN is formed. The *d*-spacing of the (111) planes plotted in **Figure 1(d)** was calculated from the 111 peak positions, with the peak fitting details shown in **Figure S1**. The results show a marked increase in the f_{N2} region from 2 to 3 sccm, further supporting the hypothesis of a nitrogen-deficient state of the CrN lattice in the low f_{N2} region, consistent with the RBS results. No secondary phases were detected, indicating that the small amount of oxygen incorporated into the films does not significantly alter the crystal structure.

Figure 1(e) shows the temperature dependence of the Seebeck coefficient for CrN(O) films deposited under different f_{N2} conditions. The films deposited with $f_{N2} \leqq$ 3 sccm exhibit *n*-type semiconductor behavior with a negative Seebeck coefficient, consistent with previous reports. [15,32] The Seebeck coefficient ranges from approximately –7 to –30 μV/K at 250 K and remains nearly constant with increasing temperature, the values of which are significantly smaller than the typical stoichiometric CrN value of around –120 μV/K at 300 K. The reduced absolute value can be attributed to the higher carrier concentration in nitrogen-deficient CrN films, as described by the Mott–Boltzmann relation:

$$S = \frac{8\pi^2 k_B^2 T}{3eh^2} m^* \left(\frac{\pi}{3n_i}\right)^{\frac{2}{3}} \qquad (1)$$

where k_B is the Boltzmann constant, h the Planck's constant, T the temperature, m^* the effective mass, e the elementary charge and n_i the carrier concentration. As indicated by this equation, the Seebeck coefficient is inversely proportional to the carrier concentration and directly proportional to the effective mass, which will be discussed in detail later. In contrast, films deposited at $f_{N2} \geqq$ 4 sccm exhibited a positive Seebeck coefficient, indicating *p*-type conduction. This result strongly suggests that the residual oxygen naturally present in the sputtering chamber, modulated by f_{N2}, can effectively be used to tune the conduction type of CrN(O) films. Interestingly, this *p*-type behavior induced by oxygen incorporation differs from previous studies. In early reports, oxygen doping was shown to suppress the Seebeck coefficient in *n*-type CrN films.[33,34]This effect is primarily attributed to electron doping: when oxygen substitutes for nitrogen in already *n*-type CrN; oxygen incorporation introduces additional electrons, thereby increasing the electron carrier concentration and reducing the Seebeck coefficient. Moreover, McGahay et al. has

 This journal is © The Royal Society of Chemistry 20xx

Please do not adjust margins

View Article Online
DOI: 10.1039/D5TA10861C

reported that, substituting nitrogen with oxygen on anion sites of CrN results in *n*-type doping which, however, is partially compensated by the formation of negatively charged Cr vacancies acting as acceptors.[35] Febvrier et al. further demonstrated that the carrier type in CrN is governed by the Cr/N ratio, and that even a small amount of oxygen incorporation can shift the apparent *n–p* transition away from the ideal stoichiometric limit.[28] In this work, however, oxygen incorporation led to both conduction-type inversion and an enhancement in the Seebeck coefficient.

We further measured cross-sectional TEM of N-deficient and Cr-deficient CrN(O) thin films to investigate possible microstructure changes. **Figure 2 (a)** and **(c)** show bright field cross-sectional TEM images of CrN(O) film deposited at a f_{N2} of 2 sccm ($CrN_{0.72}O_{0.11}$, *n*-type) and 6 sccm ($CrN_{0.93}O_{0.18}$, *p*-type), indicating that both films exhibit a columnar-like grain microstructure. The surfaces of both films are relatively smooth. **Figure 2 (b)** and **(e)** show selected area electron diffraction (SAED) patterns of the films, showing a ring pattern typical of the polycrystalline phase. Both N-deficient and Cr-deficient CrN(O) films were determined to be a single NaCl-cubic CrN phase. From the lattice spacing analysis of each crystalline plane, it is evident that upon further increases in f_{N2}, nitrogen atoms gradually occupy nitrogen-vacancy sites, resulting in an overall lattice expansion. This trend is consistent with the XRD results, where the diffraction peaks systematically shift toward lower 2θ values. In addition, as shown in **Figure 2(c)** and **(f)**, high-resolution Scanning Transmission Electron Microscopy (STEM) images reveal clear lattice fringes, further confirming that both *n*- and *p*-type CrN(O) films possess well-crystallized microstructures despite compositional differences. The chemical bonding states of both films were also characterized by XPS and with the results shown in **Figure S2**. It was found that both Cr2$p_{3/2}$ and Cr2$p_{1/2}$ peaks could be separated into two peaks using Gaussian fitting for the $CrN_{0.93}O_{0.18}$ film. The peaks at 574.83 eV and 584.28 eV are identified as Cr^{3+} due to the presence of Cr-N bonds, while the peaks at higher energy of 576.43 eV and 586.35 eV can be regarded as oxidized peaks due to the stronger binding energy of Cr-O. The N1*s* peak at 397.38 eV may indicate that the N is bonded with Cr atoms. The appearance of the O1*s* peak even after the removal of the surface oxidation layer also suggests the existence of O atoms. However, no obvious peak shift can be found between *n*-type $CrN_{0.72}O_{0.11}$ and *p*-type $CrN_{0.93}O_{0.18}$ films. Since no significant changes in the crystal structure were observed upon oxygen incorporation by XRD, TEM and XPS, more sensitive tools were employed such as synchrotron XAFS spectroscopy to further investigate the local structural variations and defect configurations responsible for the observed *p–n* conversion.

Febvrier et al. have shown that Cr vacancies introduce hole carriers and shift the Fermi level toward the valence band, giving rise to *p*-type conduction.[28] Our observation that films deposited at $f_{N2} \geqq 4$ sccm exhibit *p*-type behavior is therefore plausibly explained by a high concentration of Cr vacancies in these Cr-deficient films. To

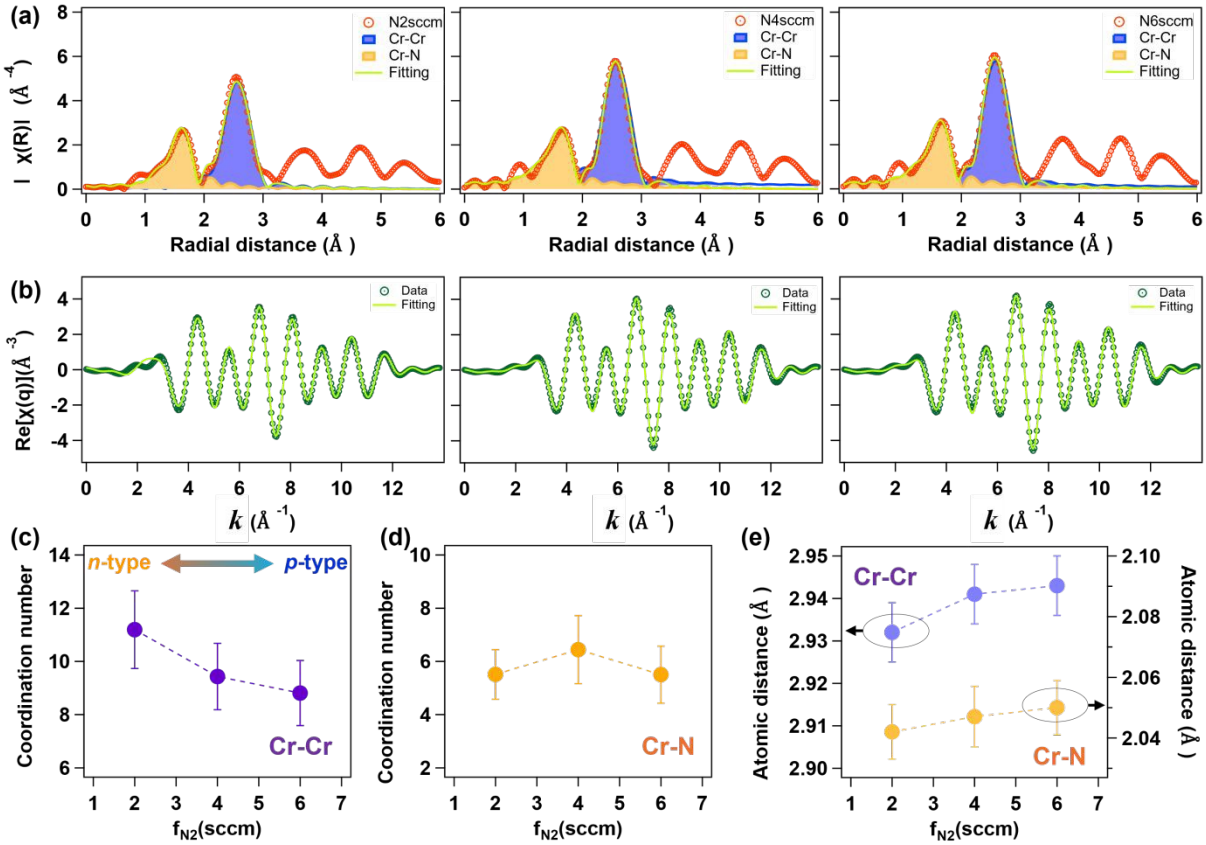

Figure 3. (a) Fourier transformed EXAFS data at the Cr K-edge and fitting results for CrN(O) films deposited at f_{N2} of 2, 4, and 6 sccm. **(b)** Experimental and simulated Back-Fourier transformed EXAFS spectra of the CrN(O) films deposited at f_{N2} of 2, 4, and 6 sccm. The simulated coordination number of **(c)** Cr-Cr and **(d)** Cr-N paths. **(e)** The atomic distances of Cr-Cr and Cr-N paths.

Open Access Article. Published on 06 March 2026. Downloaded on 3/7/2026 11:28:15 PM.
This article is licensed under a Creative Commons Attribution 3.0 Unported Licence.

Journal of Materials Chemistry A Accepted Manuscript

Please do not adjust margins

View Article Online
DOI: 10.1039/D5TA03696C

Open Access Article. Published on 06 March 2026. Downloaded on 3/7/2026 11:28:15 PM.
This article is licensed under a Creative Commons Attribution 3.0 Unported Licence.

Journal of Materials Chemistry A Accepted Manuscript

directly probe this hypothesis, we examined the local coordination of Cr in films deposited at f_{N2} =2, 4, and 6 sccm by Cr K-edge extended X-ray absorption fine structure (EXAFS). **Figure 3a** displays the Fourier transform (FT) of the k^3-weighted χ (R) spectra (plotted versus radial distance R). No secondary crystalline phases other than NaCl-type cubic CrN were detected in XRD, and the χ (R)-R spectra differed markedly from those of chromium oxides. Note that the distances show in **Figure 3a** are shorter than the crystalliographic distances due to the presence of phase shifts. The phase shifts were accounted for in the fitting process. Accordingly, we assigned the first-nearest-neighbour peak to the Cr–N shell (nominal R_{Cr-N}~ 2.08 Å, coordination number (CN)~6) and the second-neighbour peak to the Cr–Cr shell (nominal R_{Cr-Cr}~ 2.95 Å, CN~12).[36] The Cr–O scattering path was not considered in the fitting, as its inclusion did not improve but instead degraded the fitting quality, consistent with our previous report.[37] With increasing f_{N2}, the Cr–N peak position and intensity remain nearly unchanged, whereas the Cr-Cr peak intensity increased noticeably, suggesting a variation in Cr-Cr coordination. Because the EXAFS peak intensity is directly related to the CN, we quantitatively analysed these changes by fitting the χ (R) spectra in R-space range of 1-3 Å, as shown in **Figure 3a**. The best fit was done for this plot within the *k*-range of 3-12 Å (**Figure 3b**) The extracted local structural parameters are summarized in **Figure 3(c-e)** and **Table 2**.

Table 2. Curve fitting results of Cr K-edge EXAFS in the CrN(O) films deposited at f_{N2} of 2, 4, 6 sccm.

f_{N2} (sccm)	Path	Coordination Number, CN	Atomic distance (Å), R	Debye-Waller factor, σ^2	Reduced, χ^2
2	Cr-Cr	11.19 ± 1.46	2.932 ± 0.007	0.008	80.69
	Cr-N	5.51 ± 0.93	2.042 ± 0.009	0.005	
4	Cr-Cr	9.43 ± 1.25	2.941 ± 0.007	0.008	81.32
	Cr-N	6.44 ± 1.28	2.047 ± 0.010	0.006	
6	Cr-Cr	8.81 ± 1.22	2.943 ± 0.007	0.007	62.09
	Cr-N	5.50 ± 1.07	2.050 ± 0.009	0.005	

The fitted Cr-N coordination number remains near the theoretical value (~6) and shows only minor fluctuations with f_{N2}, indicating that the local octahedral Cr-N environment is largely preserved. (**Figure 3(d)**) In contrast, the Cr–Cr coordination number systematically decreases with increasing f_{N2}, reaching ~8.8 at f_{N2} = 6 sccm (from the ideal 12), which unambiguously indicates a significant concentration of Cr vacancies (Cr-site deficiency) in the high- f_{N2} films. (**Figure 3(c)**) This result is consistent with our previous transmission-mode EXAFS study on films deposited under the same conditions (f_{N2} = 6 sccm) on Al foil, which also evidenced reduced Cr–Cr coordination.[37] As the f_{N2} increases, leading to oxygen incorporation, both Cr-N and Cr-Cr bond lengths slightly increase. (**Figure 3(e)**) We attribute this to substitutional oxygen on nitrogen sites (O_N), which is thermodynamically favoured over interstitial occupation. Substitutional O_N leads to local charge redistribution and lattice relaxation, producing slight increases in Cr-N and Cr-Cr bond lengths on the order of ~0.01–0.03 Å. These local structural changes are directly linked to the electronic structure and *p*-type conduction mechanism. In ideal CrN, three nonbonding 3d electrons remain localized around the Cr atom, resulting in limited intrinsic conductivity. The introduction of Cr vacancies decreases the electron occupation of the Cr3*d* states at the vacant sites, generating localized hole states predominantly in the Cr*3d*-N*2p* hybridized bands, which act as *p*-type carriers. Oxygen substitution further modifies these states: due to its higher electronegativity, oxygen enhances Cr*3d*-O*2p* hybridization, altering the local electronic density and slightly raising the 3*d* energy levels, thereby stabilizing hole states and increasing their concentration. Simultaneously, the Cr-Cr and Cr-N bond elongation narrows the 3*d* bandwidth, enhancing electron localization and facilitating the formation and detection of additional unoccupied states.

Cr K-edge x-ray absorption near edge structure (XANES) confirms this picture, as the emergence of a new pre-edge peak (corresponds to the 1*s* → 3*d* transition) around 5992 eV indicates an increase in unoccupied 3*d* states corresponding to these localized holes. These unoccupied states directly reflect the presence of localized holes on Cr sites: the absence of electrons in the 3*d* orbitals allows 1*s* core electrons to be excited into these vacant states. Therefore, the pre-edge intensity provides a direct probe of the formation and concentration of Cr3*d* holes induced by defects or oxygen substitution. (**Figure 4**)

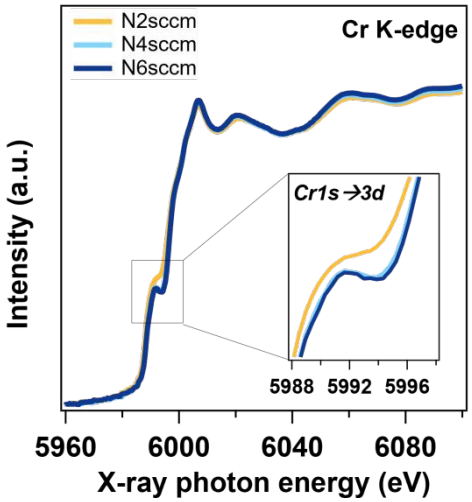

Figure 4. XANES spectra at the K-edge of CrN(O) films at f_{N2} = 2, 4, and 6 sccm.

Together, the EXAFS and XANES observations demonstrate that Cr vacancies and oxygen-induced local electronic structure modifications collectively generate hole carriers, providing a microscopic explanation for the observed *p*-type conduction in Cr-deficient, oxygen-corporate CrN films.

Electrical transport analysis

We further investigated the thermoelectric properties. **Figure 5(a)** summarized the R.T. Seebeck coefficient of films deposited at various f_{N2} as already shown in **Figure 1e**. Films deposited at low f_{N2} (1–3 sccm) exhibit negative Seebeck coefficients, and all films deposited at f_{N2} higher than 4 sccm display positive Seebeck coefficients with

This journal is © The Royal Society of Chemistry 20xx

Please do not adjust margins

View Article Online
DOI: 10.1039/D5TA10269C

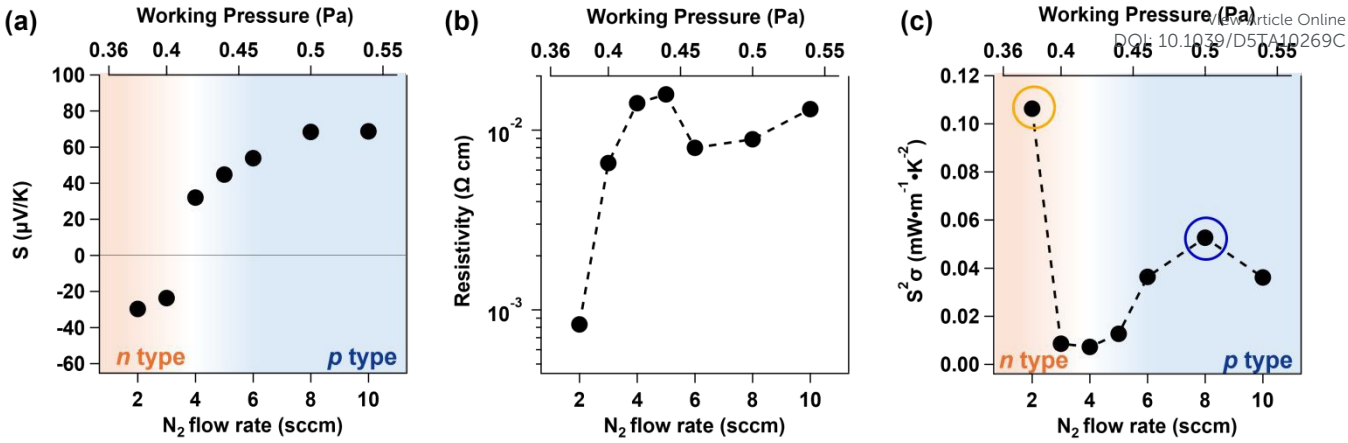

Figure 5. (a) Seebeck coefficient, **(b)** resistivity and **(c)** power factor of the CrN(O) films at various N_2 gas flow rates, f_{N2} at R.T.

significantly larger absolute values. The Seebeck coefficient increases from 36.1 μV K^{-1} to 68.8 μV K^{-1} with increasing f_{N2} from 4 to 8 sccm and saturates. In contrast to the *n*-type CrN films, where the Seebeck coefficient can be reasonably described by the Mott–Boltzmann expression (**Equation 1**) derived under the assumption of the presence of itinerant electrons in a parabolic band, the *p*-type behavior observed here arises from vacancy-related, localized hole states associated with Cr vacancies. Since these holes are strongly localized, the concept of an effective mass is not strictly applicable. Accordingly, the enhancement of the Seebeck coefficient is better interpreted within the general Mott relation, which relates the Seebeck coefficient to the energy dependence of the electronic states near the Fermi level, rather than solely to the effective mass. This framework captures the qualitative effect of oxygen incorporation and vacancy stabilization on the electronic structure and is consistent with the observed increase in the Seebeck coefficient. **Figure 5(b)** presents the R.T. resistivity as measured by van der Pauw method. The resistivity rises sharply from 8.40 × 10^{-4} Ω·cm to a maximum of 1.58 × 10^{-2} Ω·cm in the f_{N2} range below 5 sccm, followed by a slight decrease to 7.96 × 10^{-3} Ω·cm for higher f_{N2}.The corresponding power factor (PF= $S^2\sigma$), as shown in **Figure 5(c)**, reaches the maximum values of 0.105 mW·m^{-1}·K^{-2} in the *n*-type $CrN_{0.72}O_{0.11}$ (f_{N2} = 2 sccm) and 0.053 mW·m^{-1}·K^{-2} in the *p*-type $CrN_{0.93}O_{0.27}$ (f_{N2} = 8 sccm). These values are larger than some bulk CrN materials, such as *n*-type bulk CrN with PF values of around 0.03 mW·m^{-1}·K^{-2} according to ref. [26] and 0.02 mW·m^{-1}·K^{-2} for ref.[11] at R.T.; these values are a little bit lower than the reported highest *n*-type CrN films with a PF value of around 0.15 mW·m^{-1}·K^{-2} at R.T. [15]. In addition, the PF value of *p*-type $CrN_{0.93}O_{0.27}$ film at R.T. is comparable with that reported for a *p*-type $Cr_{0.96}Al_{0.04}N_{1.17}$ film which had a PF of 0.05 mW·m^{-1}·K^{-2} [26]. To further assess the thermoelectric performance, thermal conductivity measurements were performed on the representative *n*-type ($CrN_{0.72}O_{0.11}$) and *p*-type ($CrN_{0.93}O_{0.18}$) films exhibiting high PF values. The *n*-type CrN(O) film shows a thermal conductivity of approximately 2.7 W·m^{-1}·K^{-1}, consistent with previously reported values for sputtered *n*-type CrN thin films. [15] Upon oxygen incorporation and *p*-type conversion, the thermal conductivity decreased to approximately 1.8 W·m^{-1}·K^{-1}, suggesting enhanced phonon scattering induced by oxygen-related defects and cation vacancies. Based on the measured electrical and thermal transport properties, the room-temperature *ZT* value of a *n*-type CrN(O) film is approximately 0.012, comparable to most as-deposited CrN thin films, though lower than values reported for epitaxial CrN films subjected to high-temperature annealing. [15,38] The R.T. *ZT* value of the *p*-type film was 0.006 at R.T. . To the best of our knowledge, the thermal conductivity and ZT values for *p*-type CrN thin films are reported here for the first time. This demonstrates that controlled oxygen incorporation and the engineering of Cr vacancies can effectively tune carrier type while maintaining competitive thermoelectric performance.

To understand the conduction mechanisms in detail, temperature-dependent resistivity, carrier concentration, and Hall mobility were measured from 250 to 400 K in the representative *n*-type CrN(O) ($CrN_{0.72}O_{0.11}$, f_{N2} = 2 sccm) and *p*-type CrN(O) ($CrN_{0.93}O_{0.27}$, f_{N2} = 8 sccm) films. (**Figure S3(d-f)**) Both films display a negative temperature coefficient of resistivity, confirming semiconducting behavior. The Hall-effect measurements reveal that, for the *n*-type CrN(O) film, the carrier concentration increased monotonically with temperature while the Hall mobility decreases gradually, indicating that conduction is dominated by thermally activated free electrons with mobility limited by lattice or impurity scattering. The large amount of N vacancies in the film results in a higher electron concentration of $\mathbf{9.59 \times 10^{22}\ cm^{-3}}$ over that of a typical stoichiometric CrN film (order of $\mathbf{10^{20}\ cm^{-3}}$), which may lead to a reduction of the Seebeck coefficient larger than bulk CrN as mentioned in **equation 1**. In contrast, the *p*-type CrN(O) film exhibits nearly constant carrier concentration but increasing Hall mobility with temperature, consistent with conduction mediated by localized hole states formed near Cr vacancies and through Cr-O hybridized orbitals. The temperature-dependent increase in mobility can be attributed to hopping conduction of these localized holes: as the temperature rises, thermal energy facilitates the hopping between neighboring localized states, enhancing mobility. The absolute mobility of these holes is much lower, by approximately two orders of magnitude than that of the *n*-type electrons in CrN, reflecting the difference between narrow-band, localized hopping transport and wide-band, quasi-free electron conduction.

Open Access Article. Published on 06 March 2026. Downloaded on 3/7/2026 11:28:15 PM.
This article is licensed under a Creative Commons Attribution 3.0 Unported Licence.

Journal of Materials Chemistry A Accepted Manuscript

Please do not adjust margins

View Article Online
DOI: 10.1039/D5TA10269C

Open Access Article. Published on 06 March 2026. Downloaded on 3/7/2026 11:28:15 PM.
This article is licensed under a Creative Commons Attribution 3.0 Unported Licence.

Journal of Materials Chemistry A Accepted Manuscript

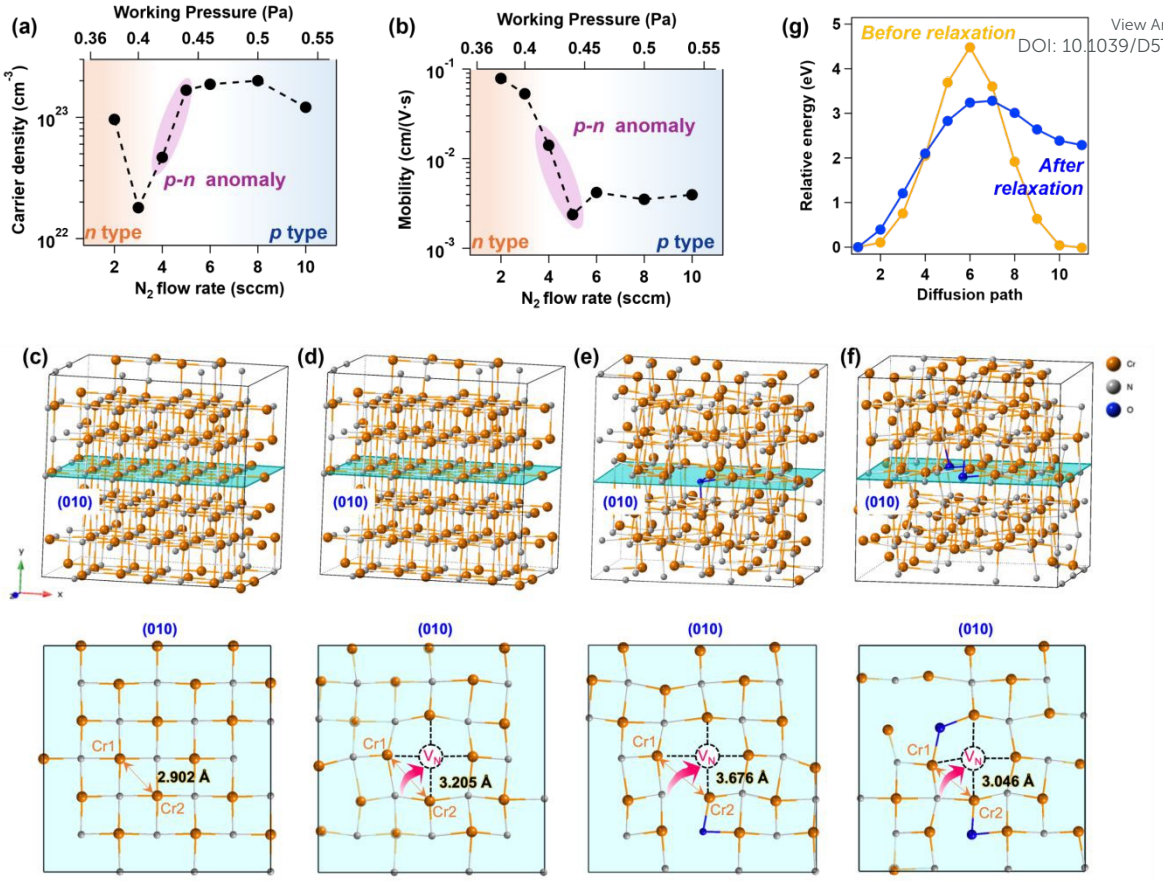

Figure 6. (a) Carrier density and **(b)** mobility of the CrN(O) films deposited at various N_2 gas flow rate, f_{N2} at R.T. Relaxed 3 × 3 × 3 supercell of **(c)** CrN; **(d)** CrN with one N vacancy site; **(e)** CrN with one N vacancy site and one substituted O atom; **(f)** CrN with one N vacancy site and two substituted O atoms; the figures under the supercell are (010) planes chosen from the supercell near the N vacancies. **(e)** The barrier energy change of N atom as a function of the diffusion path.

Further Hall-effect measurements at R.T. across the full f_{N2} range (2-10 sccm, **Figure 6(a,b)**) reveal an evolution of carrier type. Hall-effect measurements showed that films at f_{N2} = 2-5 sccm are *n*-type conduction, whereas those at f_{N2} > 5 sccm are *p*-type conduction. Notably, films at f_{N2} = 4-5 sccm exhibit a *p-n* anomaly: the Seebeck coefficient is positive, while Hall-effect measurements indicate *n*-type carriers. First-principles calculations provide a microscopic explanation. Alling et al. reported that CrN is paramagnetic with robust local magnetic moments on Cr atoms.[39] In the present study, first-principles calculations are employed to examine local structural relaxations around point defects. Since the calculations are not intended to describe electronic band structures or magnetic excitations, the focus on defect-induced lattice distortions is expected to capture the essential structural trends relevant to the experimental observations. In **Figure 6(c)**, we present a 3 × 3 × 3 supercell of cubic CrN (Fm-3m). To explore the nitrogen vacancy diffusion process in *n*-type CrN(O), we firstly introduced a nitrogen vacancy to create a path for nitrogen diffusion, as depicted in **Figure 6(d)**. Subsequently, we placed one or two oxygen atoms near the nitrogen vacancy, as shown in **Figure 6(e,f)**. Each structure underwent full relaxation, and we selected a crystal plane (010) for examination beneath the supercell. Upon relaxation of the supercell with a nitrogen vacancy (**Figure 6(d)**), we observed that the Cr-Cr distance near the vacancy (Cr1-Cr2) increased, reducing the energy barrier for neighboring nitrogen atoms to diffuse into the vacancy. (**Figure 6(g)**). When one oxygen atom (Low oxygen content, corresponding to f_{N2} ≈ 3-5 sccm) was introduced near the nitrogen vacancy, as depicted in **Figure 6(e)**, the higher bonding energy of Cr-O caused the Cr atoms to be drawn towards the oxygen side, resulting in longer and weaker Cr-Cr bonds. The elongation of the Cr–Cr bonds soften the local lattice and lowers both the formation and migration barriers for nitrogen vacancies. Because nitrogen vacancies act as electron-donor defects in CrN, the presence of more mobile and easily ionized nitrogen vacancies increases the concentration of activated donor states, resulting in a relatively higher *n*-type carrier density CrN(O) (f_{N2}≈ 4-5 sccm). However, the concomitant lattice distortion significantly reduces carrier mobility. In this regime, high-mobility electrons dominate the Hall response, leading to *n*-type Hall measurements, while the newly formed localized hole states, which contribute strongly to the thermopower, yield a positive Seebeck coefficient. At higher oxygen concentrations (~2 O atoms, f_{N2}>5 sccm), the local formation of Cr–O bonds result in slightly shortened nearby Cr–Cr distances and suppression of long-range nitrogen-vacancy diffusion. At the same time, the increased oxygen content shifts the overall stoichiometry toward (N + O) > Cr, making charge compensation through the formation of Cr vacancies

This journal is © The Royal Society of Chemistry 20xx

View Article Online
DOI: 10.1039/D5TA10260C

energetically more favorable than through nitrogen vacancies. (**Figure 6(f)**) This stabilizes the localized hole states, resulting in *p*-type conduction for both Seebeck and Hall-effect measurements. EXAFS and XANES corroborate this picture: Cr-Cr bond lengths increase with oxygen incorporation, coordination numbers decrease, and the Cr K-edge XANES pre-edge peak grows, confirming the formation of localized unoccupied 3*d* states. Temperature-dependent mobility trends further support the transport interpretation: *n*-type films are electron-dominated with mobility decreasing at higher temperatures, while *p*-type films exhibit activation-dominated hole transport via localized states. The correlation between microscopic defects, localized electronic states, and macroscopic transport properties illustrates that careful tuning of f_{N2} (oxygen content) enables controlled carrier type and optimized thermoelectric performance in CrN(O) films.

Conclusions

In conclusion, *p*-type CrN(O) films have been successfully developed by incorporating residual oxygen impurities during RF magnetron sputtering through careful regulation of N_2 gas flow control. At low f_{N2}, the N/Cr atomic ratio was less than 1, leading to N-deficient CrN(O) films in which nitrogen vacancies dominate, resulting in *n*-type conduction. As f_{N2} is increased over 4 sccm, the N/Cr ratio approached unity, but oxygen incorporation simultaneously occurred, producing over-stoichiometric CrN(O) films with a total (O+N)/Cr ratio greater than 1. In these films, Cr vacancies were generated and stabilized, giving rise to *p*-type hole conduction. The optimal compositions for thermoelectric performance were identified as $CrN_{0.72}O_{0.11}$ for *n*-type and $CrN_{0.93}O_{0.27}$ for *p*-type films, exhibiting the highest R.T. power factor values.

Structural and spectroscopic analyses revealed that both *n*- and *p*-type films possess similar NaCl-type cubic microstructures, with subtle variations in Cr-Cr bond lengths, local coordination, and Cr3*d*-O/N2*p* hybridization, which underpin the observed carrier type and transport properties. The coexistence of these *n*- and *p*-type films with comparable crystal structures provides a promising platform for the formation of *p*–*n* homojunctions, potentially enabling integrated thermoelectric devices with improved compatibility and efficiency. These findings demonstrate a straightforward and controllable strategy to achieve both *n*- and *p*-type CrN(O) films, linking defect engineering, oxygen incorporation, and carrier type control, and open new avenues for nitride film thermoelectric applications.

Conflicts of interest

There are no conflicts to declare.

Acknowledgements

This work was supported by JSPS KAKENHI (Grant Nos. 24K00915 and 21H05009), the Thermal & Electric Energy Technology Foundation (TEET) and the FY2023 Fusion Research Funds from WPI-AIMR, Tohoku University. The authors acknowledge financial support from the JST FORESTP Program, Grant No. JPMJFR235T. This work was supported by the WAKASAPO program of the New Energy and Industrial Technology Development Organization (NEDO), Japan. The authors thank Dr. T.Miyazaki, (Tohoku University, Japan) for their technical support for the TEM measurements.

Notes and references

1. F. J. Disalvo, *Science*, 1999, 285,703-706.
2. J. He and T. M. Tritt, *Science*, 2017, 357, eaak9997.
3. G. J. Snyder and E. S. Toberer, *Nature Mater*, 2008, 7, 105-114.
4. T. Deng, Z. Gao, Z. Li, P. Qiu, Z. Li, X. Yuan, C. Ming, T. R. Wei, L. Chen and X. Shi, *Science*, 2024, 386, 1112–1117.
5. X. Chen, Z. Zhou, Y. H. Lin and C. Nan, *Journal of Materiomics*, 2020, 6, 494–512.
6. C. Bianchi, J. Loureiro, P. Duarte, J. Marques, J. Figueira, I. Ropio and I. Ferreira, *Adv Mater Technol*, 2016, 1, 1600077.
7. N. S. Hudak and G. G. Amatucci, *J Appl Phys*, 2008, 103, 101301.
8. S. H. Choday, M. S. Lundstrom and K. Roy, *IEEE Trans Compon Packaging Manuf Technol*, 2013, 3, 2059–2067.
9. P. Mannu, M. Palanisamy, G. Bangaru, S. Ramakrishnan, R. Meena, C. L. Dong and A. Kandasami, *Appl Surf Sci*, 2020, 505, 144115.
10. R. Lan, S. L. Otoo, P. Yuan, P. Wang, Y. Yuan and X. Jiang, *Appl Surf Sci*, 2020, 507, 145025.
11. C. X. Quintela, F. Rivadulla and J. M. Rivas, *Appl Phys Lett*, 2009, 94, 152103.
12. P. Eklund, S. Kerdsongpanya, B. Rn and A. Ab, *J. Mater. Chem. C*, 2016, 4, 3905.
13. S. Kerdsongpanya, N. Van Nong, N. Pryds, A. Žukauskaite, J. Jensen, J. Birch, J. Lu, L. Hultman, G. Wingqvist and P. Eklund, *Appl Phys Lett*, 2011, 99, 232113.
14. A. Le Febvrier, N. Tureson, N. Stilkerich, G. Greczynski and P. Eklund, *J Phys D Appl Phys*, 2019, 52, 035302.
15. C. X. Quintela, J. P. Podkaminer, M. N. Luckyanova, T. R. Paudel, E. L. Thies, D. A. Hillsberry, D. A. Tenne, E. Y. Tsymbal, G. Chen, C. Eom and F. Rivadulla, *Advanced Materials*, 2015, 27, 3032–3037.
16. M. A. Gharavi, S. Kerdsongpanya, S. Schmidt, F. Eriksson, N. V. Nong, J. Lu, B. Balke, D. Fournier, L. Belliard, A. Le Febvrier, C. Pallier and P. Eklund, *J Phys D Appl Phys*, 2018, 51, 355302.
17. B. Wei, H. Liang, D. Zhang, Z. Wu, Z. Qi and Z. Wang, *J Mater Chem A Mater*, 2017, 5, 2844–2851.
18. X. Y. Zhang, J. S. Chawla, B. M. Howe and D. Gall, *Phys Rev B Condens Matter Mater Phys*, 2011, 83, 165205.
19. S. Lee, K. Esfarjani, T. Luo, J. Zhou, Z. Tian and G. Chen, *Nat Commun*, 2014, 5, 1–8.
20. M. Novaković, M. Popović, Z. Rakočević and N. Bibić, *Processing and Application of Ceramics*, 2017, 11, 45–51.
21. A. Garzon-Fontecha, H. A. Castillo, E. Restrepo-Parra and W. De La Cruz, *Surf Coat Technol*, 2018, 334, 98–104.
22. D. Gall, C. S. Shin, R. T. Haasch, I. Petrov and J. E. Greene, *J Appl Phys*, 2002, 91, 5882–5886.
23. A. Herwadkar and W. R. L. Lambrecht, *Phys Rev B Condens Matter Mater Phys*, 2009, 79, 035125.

Open Access Article. Published on 06 March 2026. Downloaded on 3/7/2026 11:28:15 PM.
This article is licensed under a Creative Commons Attribution 3.0 Unported Licence.

Journal of Materials Chemistry A Accepted Manuscript

Please do not adjust margins

View Article Online
DOI: 10.1039/D5TA10269C

Open Access Article. Published on 06 March 2026. Downloaded on 3/7/2026 11:28:15 PM.
This article is licensed under a Creative Commons Attribution 3.0 Unported Licence.

Journal of Materials Chemistry A Accepted Manuscript

24. G. Kogo, H. Lee, A. H. Ibrahim, X. Bo, S. K. Pradhan and M. Bahoura, *J Appl Phys*, 2018, 124, 165106.
25. R. Chavez, S. Angst, J. Hall, F. Maculewicz, J. Stoetzel, H. Wiggers, L. Thanh Hung, N. Van Nong, N. Pryds, G. Span, D. E. Wolf, R. Schmechel and G. Schierning, *J Phys D Appl Phys*, 2017, 51, 014005.
26. A. Le Febvrier, N. Van Nong, G. Abadias and P. Eklund, *Applied Physics Express*, 2018, 11, 051003.
27. T. Aizawa, F. F. Yun and T. Mori, *ACS Appl. Energy Mater*, 2025, 8, 13360–13366.
28. A. Le Febvrier, D. Gambino, F. Giovannelli, B. Bakhit, S. Hurand, G. Abadias, B. Alling and P. Eklund, *Phys Rev B*, 2022, 105, 104108.
29. T. Nakano, K. Hoshi and S. Baba, *Vacuum*, 2008, 83, 467–469.
30. B. Ravel and M. Newville, in *Journal of Synchrotron Radiation*, International Union of Crystallography, 2005, 12, 537–541.
31. N. Jiang, D. G. Georgiev and A. H. Jayatissa, *Semicond Sci Technol*, 2013, 28, 25009–25017.
32. S. Chowdhury, V. Hjort, R. Shu, G. Greczynski, A. Le Febvrier and M. Magnuson, *Phys Rev B*, 2051, 108, 205134.
33. P. Tomeš, D. Logvinovich, J. Hejtmánek, M. H. Aguirre and A. Weidenkaff, *Acta Mater*, 2011, 59, 1134–1140.
34. O. Jankovský, D. Sedmidubský, Š. Huber, P. Šimek and Z. Sofer, *J Eur Ceram Soc*, 2014, 34, 4131–4136.
35. M. E. McGahay, S. V. Khare and D. Gall, *Phys Rev B*, 2020, 102, 235102.
36. Y. Tripathi, R. Gupta, Seema, M. Gupta, D. M. Phase and P. Rajput, *Thin Solid Films*, 2019, 670, 113–121.
37. Y. Shuang, S. Mori, T. Yamamoto, S. Hatayama, Y. Saito, P. J. Fons, Y. H. Song, J. P. Hong, D. Ando and Y. Sutou, *ACS Nano*, 2024, 18, 21135–21143.
38. B. Biswas, S. Chakraborty, O. Chowdhury, D. Rao, A. I. K. Pillai, V. Bhatia, M. Garbrecht, J. P. Feser and B. Saha, *Phys. Rev. Mater.*, 2021, 5, 114605.
39. B. Alling, T. Marten and I. A. Abrikosov, *Phys. Rev. B*, 2010, 82, 184430.

This journal is © The Royal Society of Chemistry 20xx

Please do not adjust margins

View Article Online
DOI: 10.1039/D5TA10269C

Data Availability Statement

The data supporting the findings of this study are available within the article and from the corresponding author upon reasonable request.

Open Access Article. Published on 06 March 2026. Downloaded on 3/7/2026 11:28:15 PM.
This article is licensed under a Creative Commons Attribution 3.0 Unported Licence.

Journal of Materials Chemistry A Accepted Manuscript